

# A comparative study: The effect of current loading modes on the cold start-up process of PEMFC stack

Le Lei, Pu He, Peng He, Wen-Quan Tao\*

Shaanxi Collaborative Innovation Center for PEMFC Performance Improvement, Key Laboratory of Thermal Fluid Science and Engineering of MOE, School of Energy and Power Engineering, Xi'an Jiaotong University, Xi'an, Shaanxi 710049, PR China

## ARTICLE INFO

### Keyword:

PEMFC  
Cold start-up  
Current loading modes  
Stepwise-changed mode

## ABSTRACT

The start-up of the proton exchange membrane fuel cell (PEMFC) at temperatures below the freezing point is considered one of the major obstacles hindering the widespread commercialization applications of fuel cells. In this work, a one-dimensional transient numerical model is adopted to study the effects of five different current loading modes on the stack start-up from  $-20\text{ }^{\circ}\text{C}$ . They are constant current loading mode, constant slope ramp loading mode, variable slope ramp loading mode, zigzag current loading mode, and stepwise-changed current loading mode. The detailed comparative analyses are presented for a better understanding of the cold start-up process. Three levels (good, appropriate, and inferior) are used to evaluate the performance of the current loading modes. The results show that the stepwise-changed current loading mode is the best among the five modes because it has the advantages of appropriate start-up time, temperature rising rate, ohmic resistance, heat generation rate, ice volume fraction, and water production rate.

## 1. Introduction

The proton exchange membrane fuel cell (PEMFC) is an energy conversion device using hydrogen and air as fuel gas. The products are only pure water and electric power, thus it is widely used in the new energy automobile industry [1–4]. With the support of government policies and environmental protection requirements, the fuel cell vehicle industry ushered in a flourishing market worldwide. One of the vital obstacles hindering the large-scale commercial application of fuel cell vehicles is cold start-up under a winter sub-freezing temperature [5–8]. In subzero weather, the product water will change into ice and then occupies the pores of the porous layers [9–12]. And the freezing of water may result in the PEMFC output performance deteriorating seriously and the structure of porous layers being destroyed. It is necessary to study how to conduct each cold start-up successfully to reduce the degree of performance degradation and structural damage to the minimum. Therefore, for different power stacks of PEMFC, the study on an optimal strategy for the cold start-up is indispensable.

Many significant works have been carried out to explore a proper and optimal cold start-up strategy. So far, the cold start-up strategy can be broadly classified into two categories: self-start-up and assisted start-up. In the self start-up category, as reported in Ref. [13–15], the constant

power, constant current, and constant voltage modes are the three most widely used start-up modes. Yang et al. [15] experimentally investigated the effects of operating conditions on the PEMFC cold start-up based on the constant voltage mode. And optimized operating conditions used in the constant voltage mode are obtained. Du et al. [16] explored a max power mode based on a multiphase PEMFC stack model. By comparing with the three basic start-up modes mentioned above, they found that the max power mode is the optimal for the cold start-up of the PEMFC studied. Amamou et al. [17,18] proposed an internal-based adaptive strategy to control the PEMFC stack to maximize the generated heat and power. Compared with the constant current and constant voltage modes, the proposed approach has a superior performance. Recently, Zang et al. [19] studied different current density operation modes based on a simplified one-dimensional numerical model of a single PEMFC and obtained the current density threshold for the successful cold start-up corresponding to the researched modes.

Except for the above-mentioned self-starting strategy, the assisted cold start-up strategy is also extensively reported in literatures. Sun et al. [20] developed a cold start-up procedure that made hydrogen and oxygen react to heat the fuel cell. By controlling the  $\text{H}_2$  concentration and gas flow rate in the experiments, the cell temperature rose quickly and stably, finally causing a successful cold start-up. Guo et al. [21] implemented the anode hydrogen–oxygen catalytic reaction in a three-

\* Corresponding author.

E-mail address: [wqtao@mail.xjtu.edu.cn](mailto:wqtao@mail.xjtu.edu.cn) (W.-Q. Tao).

Nomenclature	
$a$	water activity
$A$	effective activation area, $m^2$
$ASR$	area-specific resistance, $\Omega m^2$
$C$	mole concentration, $mol m^{-3}$
$c_{nfm}$	mole concentration of the none-frozen membrane water, $mol m^{-3}$
$c_p$	specific heat capacity, $J kg^{-1} K^{-1}$
$D$	diffusivity, $m^2 s^{-1}$
$EW$	equivalent weight of membrane, $kg mol^{-1}$
$F$	Faraday's constant, $C mol^{-1}$
$h$	convective heat transfer coefficient, $W m^{-2} K^{-1}$
$I$	current, A
$j_s$	exchange current density, $A cm^{-2}$
$k$	thermal conductivity, $W m^{-1} K^{-1}$
$K$	permeability, $m^2$
$M$	molecular weight, $kg mol^{-1}$
$n$	number of the current loading cycle
$p$	pressure, Pa
$Q$	quantity of generated heat, $J cm^{-2}$
$R$	universal gas constant, $J mol^{-1} K^{-1}$
$s$	volume fraction
$S$	mass sources terms
$t$	time, s
$T$	temperature, K
$V$	the output voltage, V
<i>Greek letters</i>	
$\alpha$	current loading slope in Case-2, Case-3, and Case-5
$\beta$	current loading slope in Case-4
$\gamma$	water transfer rate
$\delta$	thickness, mm
$\epsilon$	porosity
$\zeta$	water transfer rate, $s^{-1}$
$\kappa$	intrinsic permeability, $m^2$
$\lambda$	water content
$\mu$	dynamic viscosity, $kg m^{-1} s^{-1}$
$\xi$	stoichiometry ratio
$\rho$	density, $kg m^{-3}$
$\sigma$	electric conductivity, $S m^{-1}$
$\omega$	volume fraction of ionomer
<i>Subscripts and superscripts</i>	
$a$	anode
$act$	activation
$bp$	bipolar plate
$c$	cathode
$cell$	cell characteristic
$cycle$	the time cycle of current loading
$CL$	catalyst
$conc$	concentration
$eff$	effective
$eq$	equilibrium
$f$	frozen
$fl$	fluid phase
$fm$	frozen membrane water
$g$	gas phase
$GDL$	gas diffusion layer
$H_2O$	water
$i$	the $i$ th phase of water
$ice$	ice
$j$	the $j$ th phase of water
$load$	current loading
$lq$	liquid water
$mem$	membrane
$nernst$	nernst
$nfm$	none-frozen membrane water
$ohmic$	ohmic
$out$	output
$P$	power
$sat$	saturation
$sl$	solid phase
$stack$	stack characteristic
$T$	energy (source term)
$threshold$	threshold value
$vp$	vapor
$wall$	surrounding wall of the stack

dimensional cold start-up model of a single cell and achieved a successful cold start-up from  $-20^\circ C$ . Luo et al. [22] developed a one-dimensional PEMFC stack model with the hydrogen–oxygen catalytic reaction both in anode and cathode. The anode catalytic reaction with optimized reactants concentration was recommended for the PEMFC stack cold start-up. Another assistance strategy is preheating by the external energy, say electrical heating [23], before the cold start-up. Zhan et al. [24] made the comparisons among endplates heating, air preheating, and coolant heating in a 2 kW PEMFC stack experiments, and the endplates heating with high efficiency stood out from the crowd. Recently, Yang et al. [25] developed an integrated system model consisting of a PEMFC stack, membrane humidifier, hydrogen pump, gas compressor, and radiator. And, to get a successful cold start-up, three assisted pre-heating approaches (fuel gas heating, stack heating, and coolant heating) were adopted. They found that the power consumption for heating coolant is enormous, and the secondary power sources are necessary.

For fuel cell vehicles, the constant voltage mode, constant current mode, and constant power mode are not applicable because the conditions of a running automobile are timely changed. Also, using the hydrogen–oxygen catalytic reaction to heat the PEMFC stack may face a significant risk that the membrane may be destroyed. Besides, pre-heating before start-up is only used under a very low subzero

temperature because the method needs external electrical power and makes the stack system more complex. Hence, finding a proper and optimal unassisted strategy for the PEMFC stack cold start-up is imperative.

Numerical simulations of the PEMFC stack cold start-up process are mainly one-dimensional models [18,19,22,25–29], and three-dimensional simulation models [8,14,30,31] are only used to simulate a single cell or even a single channel [14,32] in the literature because the transient simulations in three-dimensional space would take enormous computation time. In the references mentioned above, researchers mainly pay attention to the mechanisms of the water phase transformation [26–29] and the cold up strategies, such as the self-heating [18,19] and assisted heating methods [22,25].

To the authors' knowledge, no studies have been conducted to examine different current loading modes of the PEMFC stack cold start up by comparing the output characteristics such as the temperature, ice volume fraction, inner resistance, and the requirement indexes of the cold start-up process.

The present work aims to study the effects of current loading modes on the PEMFC stack start-up process and recommend an optimal one. Hence, a transient one-dimensional cold start-up model of the PEMFC stack is proposed, and the requirements for a successful cold start-up are recommended. This is the major innovative point of the present study.

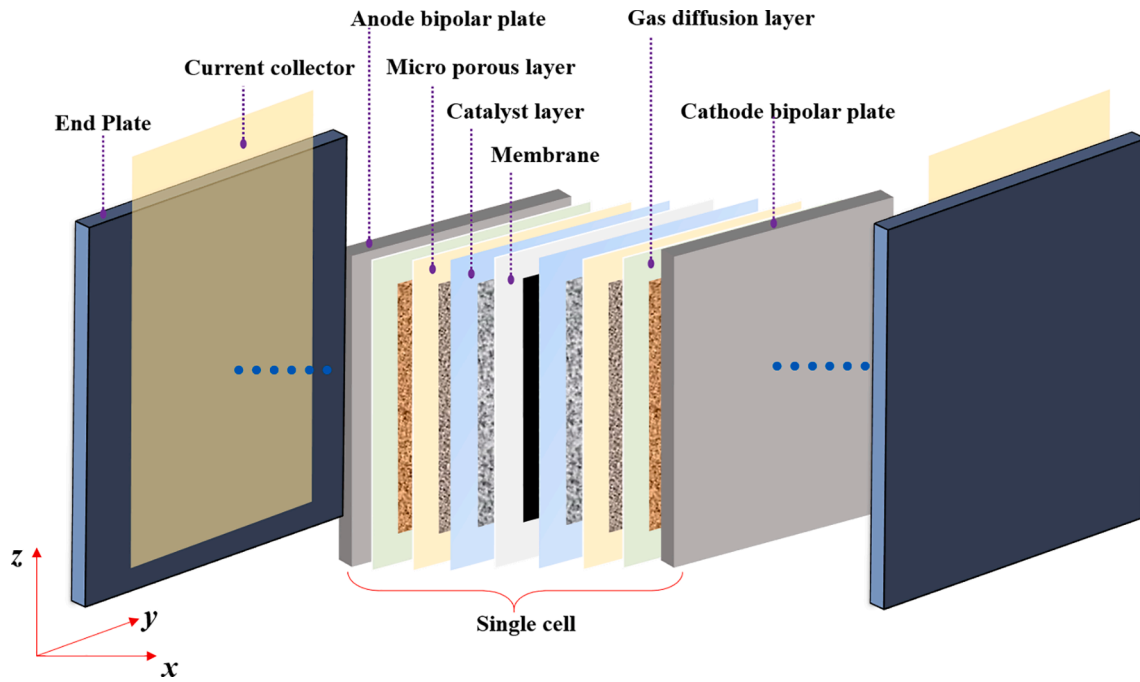


Fig. 1. Schematic diagram of PEMFC stack structure.

Table 1  
Physical parameters of the PEMFC stack.

Physical parameters	Value	Unit
The active area of the cell [33]	25	cm <sup>2</sup>
The width of the cell	5	cm
The length of the cell	5	cm
The depth of the channel	1	mm
Thickness of BP; GDL; MPL; CL; membrane [13]	2000; 200; 30; 10; 30	μm
Porosities of GDL; MPL; CL	0.7; 0.4; 0.3	
Contact angle of GDL; MPL; CL	120; 100; 100	
Intrinsic permeability of GDL; MPL; CL [34]	$6.2 \times 10^{-12}$ ; $6.2 \times 10^{-13}$ ; $6.2 \times 10^{-13}$	m <sup>2</sup>
Electrical conductivities of BP; GDL; MPL; CL [13]	25000; 300; 300; 300	S m <sup>-1</sup>
Thermal conductivities of BP; GDL; MPL; CL; mem	20; 1.5; 1.2; 1.2; 0.95	Wm <sup>-1</sup> K <sup>-1</sup>
The mass density of the BP; GDL; MPL; CL; mem [13]	1000; 1000; 1000; 1000; 1980.0	kg m <sup>-3</sup>
The equivalent weight of the membrane	1100.0	kg mol <sup>-1</sup>
The specific heat capacity of BP; GDL; MPL; CL [13]	1580; 2000; 568; 3300; 833	J kg <sup>-1</sup> K <sup>-1</sup>

Five current loading modes are adopted to study a specific cold start-up situation from  $-20\text{ }^{\circ}\text{C}$ . By comparatively analyzing the dynamic process characteristics, an optimal current loading mode is recommended.

## 2. Model descriptions

In this section, the details of the physical and mathematical models are described.

### 2.1. Physical model

A PEMFC stack consists of several single cells and two endplates (EP) which are set up at each side along the length direction to fix the stack. Every single cell contains the proton exchange membrane (PEM), catalyst layer (CL), microporous layer (MPL), gas diffusion layer (GDL), and bipolar plate (BP), as shown in Fig. 1. The physical parameters of the PEMFC stack studied in this paper are listed in Table 1.

Fig. 2 shows the water transition mechanism in a general PEMFC cell under the sub-zero and above-zero temperatures at atmosphere pressure. In the membrane, non-frozen membrane water (also called membrane water usually) will change into frozen membrane water when the temperature is below zero, and the membrane water content is larger

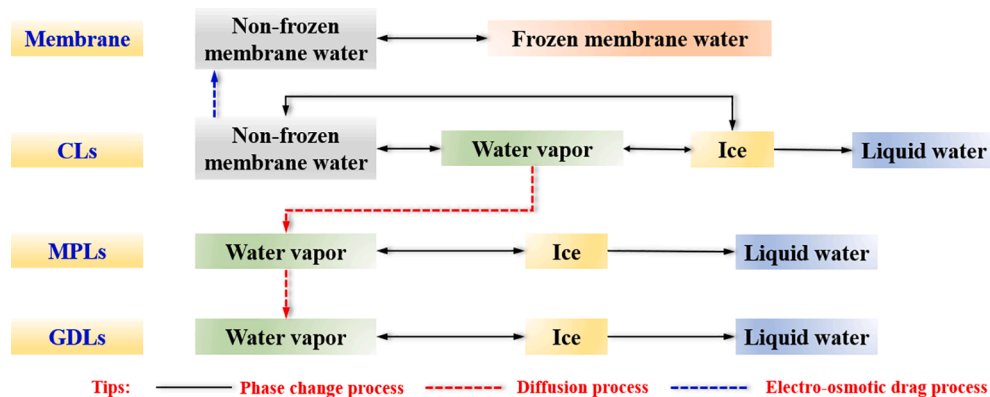


Fig. 2. Phase change mechanism in the PEMFC stack.

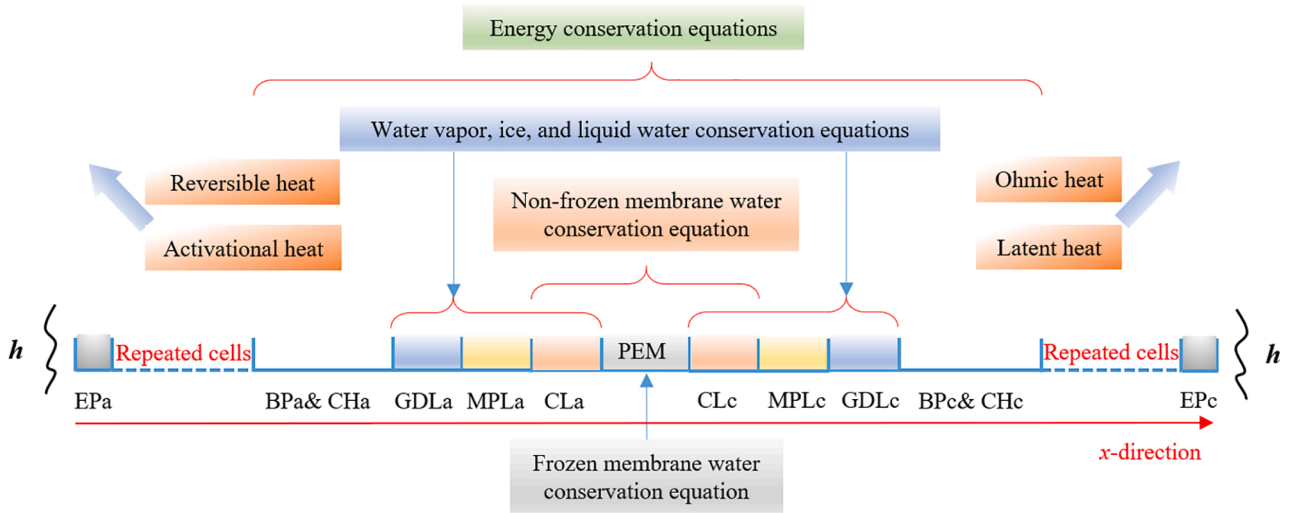


Fig. 3. Conservation equation diagram of the one-dimensional PEMFC cold start-up model.

Table 2  
Operation conditions and transport properties.

Parameters	Value/Equation	Unit
Volume fraction of ionomer in CL	$\omega_a = 0.3, \omega_c = 0.3$	
Stoichiometry ratio	$\xi_a = 2.0, \xi_c = 2.0$	
Initial stack temperature	$T_{ini} = 253.15$	K
Pressure at outlets	$p_{out} = 1$	atm
Heat transfer coefficient on endplates surface	$h = 50.0$	$W m^{-2} K^{-1}$
Heat transfer coefficient on side surfaces	$h = 2.0$	$W m^{-2} K^{-1}$
Initial ice volume fraction	0	
Initial none-frozen membrane water	6.2	
Initial frozen membrane water	0	
Phase change rate( $\gamma$ )	1.0	$s^{-1}$
Liquid water diffusivity [34]	$D_{lq} = \frac{K_{lq}}{\mu_{lq}} \frac{dp_c}{ds_{lq}}$	$m^2 s^{-1}$
Capillary pressure in porous layers [37]	$p_c = \sigma \cos(\theta) \left(\frac{\epsilon}{\kappa_0}\right)^{0.5} [1.42(1 - s_{lq}) - 2.12(1 - s_{lq})^2 + 1.26(1 - s_{lq})^3] \quad (\theta < 90^\circ)$ $p_c = \sigma \cos(\theta) \left(\frac{\epsilon}{\kappa_0}\right)^{0.5} [1.42s_{lq} - 2.12s_{lq}^2 + 1.26s_{lq}^3] \quad (\theta > 90^\circ)$	Pa
Effective permeability of liquid water [34]	$\kappa_{lq} = \kappa_0 s_{ice}^{4.0} (1 - s_{ice})^{4.0}$	$m^2$
Equivalent water content and water activity [38]	$\lambda_{eq} = \begin{cases} 0.043 + 17.81a - 39.58a^2 + 36.0a^3 & (0 \leq a < 1) \\ 14.0 + 1.4(a - 1) & (1 < a \leq 3) \end{cases} a = \frac{X_{vp} p_g}{p_{sat}} + 2s_{lq}$	
Effective volumetric heat capacities	$(\rho C_p)_{fl,sl}^{eff} = \epsilon [s_{lq} \rho_{lq} (C_p)_{lq} + s_{ice} \rho_{ice} (C_p)_{ice} + (1 - s_{lq} - s_{ice}) \rho_g (C_p)_{g}]$ $+ (1 - \epsilon - \omega) \rho_s (C_p)_s + \omega \rho_{mem} (C_p)_{mem}$	$J m^{-3} K^{-1}$
Effective thermal conductivity	$k_{fl,sl}^{eff} = \epsilon [s_{lq} k_{lq} + s_{ice} k_{ice} + (1 - s_{lq} - s_{ice}) k_g] + (1 - \epsilon - \omega) k_s + \omega k_{mem}$	$W m^{-1} K^{-1}$

than the saturated membrane water content. The water vapor and non-frozen membrane water will transform to ice under proper conditions. When the temperature rises to zero, the ice will be melted into liquid water. The water vapor will transport to porous zones such as the microporous and gas diffusion layers through the diffusion process. Both desublimation and melting processes will occur in the porous layers.

When a PEMFC is in normal operation, very complicated physical phenomena and processes occur inside the PEMFC, including fluid flow, heat and mass transfer, electronic transportation, and chemical reactions. However, in the cold start-up state, the dominated process is the diffusion of different kinds of water. These diffusion processes are considered along the through-plane direction (x-direction) in the present one-dimensional numerical model. As shown in Fig. 3, all five water phase transition processes are considered inside each cell in this model. All these mass conservation equations of different cells in the whole stack are solved simultaneously to obtain the phase distribution along the x-direction. And each cell temperature is gained by solving the energy conservation equation in the entire stack region. Besides, the convective heat transfer boundary condition with a constant heat transfer coefficient is set to the two-end surfaces of the PEMFC stack. The

detailed operation conditions and transport properties in the cold start-up model are shown in Table 2.

The basic assumptions made in this study are as follows:

- (1) The fluid flow is laminar and incompressible due to the low gas pressure and low Reynolds number [35].
- (2) The gas flow in channels is ignored;
- (3) The air and fuel gas are regarded as ideal-gas;
- (4) The gravity effect is neglected;
- (5) Only the icing process on the cathode side is considered because the membrane water is mainly produced on the cathode of the cell [13];
- (6) There is no ice inside the cell at the initial state, assuming that the liquid water is entirely purged by the purge process implemented when the stack is shut down.

It is worth noting that the first five assumptions are usual in the cold start-up study [13,19,22,36]. As for the sixth assumption, our simulation model can also study the non-zero initial ice situation without any difficulty. Zero ice fraction is only a representative among others.

## 2.2. Conservation equations

### 2.2.1. Mass transport

The amount of non-frozen membrane water in the membrane and catalytic layer can be predicted as follows. First, the governing equation for the non-frozen water content  $\lambda_{nfm}$  in the membrane and catalytic layer is solved [13,22,36]:

$$\frac{\rho_{mem}}{EW} \frac{\partial(\omega\lambda_{nfm})}{\partial t} = \frac{\rho_{mem}}{EW} \frac{\partial^2(\omega^{1.5}D_{nfm}\lambda_{nfm})}{\partial x^2} + S_{nfm} \quad (1)$$

where  $\rho_{mem}$  (kg m<sup>-3</sup>) is the density,  $EW$  (kg kmol<sup>-1</sup>) is the equivalent weight of membrane, and  $\omega$  is the volume fraction of ionomer in catalyst layer;  $S_{nfm}$  (mol m<sup>-3</sup> s<sup>-1</sup>) is the mass source term of the non-frozen membrane water, and  $D_{nfm}$  (m<sup>2</sup> s<sup>-1</sup>) is the mass diffusivity in ionomer, which is related to membrane water content and temperature. And it can be presented in the form of a piecewise function shown by Eq. (2) [39]:

$$D_{nfm} = \begin{cases} 2.69266 \times 10^{-10}, (\lambda_{nfm} \leq 2) \\ 10^{-10} \cdot \exp\left[2416\left(\frac{1}{303} - \frac{1}{T}\right)\right] \cdot [0.87(3 - \lambda_{nfm}) + 2.95(\lambda_{nfm} - 2)], (2 < \lambda_{nfm} \leq 3) \\ 10^{-10} \cdot \exp\left[2416\left(\frac{1}{303} - \frac{1}{T}\right)\right] \cdot [2.95(4 - \lambda_{nfm}) + 1.642454(\lambda_{nfm} - 3)], (3 < \lambda_{nfm} \leq 4) \\ 10^{-10} \cdot \exp\left[2416\left(\frac{1}{303} - \frac{1}{T}\right)\right] \cdot [2.563 - 0.33\lambda_{nfm} + 0.0264\lambda_{nfm}^2 - 0.0006713\lambda_{nfm}^3], (\lambda_{nfm} > 4) \end{cases} \quad (2)$$

Then the mole concentration of non-frozen membrane water in the membrane ( $C_{nfm}$ , mol m<sup>-3</sup>) can be obtained by Equation (3) [40]

$$C_{nfm} = \frac{\rho_{mem}\lambda_{nfm}}{EW} \quad (3)$$

The membrane will absorb water when the non-frozen membrane water content is less than the saturated water content ( $\lambda_{sat}$ ). The absorbing process is called the phase change process between non-frozen and frozen membranes [29]. The saturated water content is usually gained by the empirical formula derived from the experimental tests given in [41].

$$\lambda_{sat} = \begin{cases} 4.837 & (T < 223.15K) \\ [-1.304 + 0.01479T - 3.594 \times 10^{-5}T^2]^{-1} & (223.15K \leq T < T_{freeze}) \\ > \lambda_{nfm} & (T \geq T_{freeze}) \end{cases} \quad (4)$$

The frozen membrane water content in the membrane can be obtained by solving the frozen membrane water conservation equation, as shown in Eq. (5).

$$\frac{\rho_{mem}}{EW} \frac{\partial(\omega\lambda_{fm})}{\partial t} = S_{fm} \quad (5)$$

where  $\lambda_{fm}$  is the frozen membrane water content, and  $S_{fm}$  (mol m<sup>-3</sup> s<sup>-1</sup>) represents the mass source term of frozen membrane water.

The mass conservation equation of liquid water and water vapor can be expressed as Eqs. (6) and (7), respectively. It is worth noting that the discretized governing equations of the water vapor concentration are solved by the implicit scheme. Hence a much larger time step of the numerical simulations can be used compared with the explicit scheme used in Refs. [13,16,22,28].

$$\frac{\partial(\varepsilon\rho_{lq}S_{lq})}{\partial t} = \frac{\partial^2(\rho_{lq}D_{lq}S_{lq})}{\partial x^2} + S_{lq} \quad (6)$$

$$\frac{\partial(\varepsilon(1 - S_{lq} - S_{ice})\rho_g c_{vap})}{\partial t} = \frac{\partial^2(\rho_g D_{vap} c_{vap})}{\partial x^2} + S_{vap} \quad (7)$$

where  $\varepsilon$  denotes the porosity of the porous electrode,  $\rho_{lq}$  (kg m<sup>-3</sup>),  $\rho_g$  (kg m<sup>-3</sup>),  $D_{lq}$  (m<sup>2</sup> s<sup>-1</sup>),  $D_{vap}$  (m<sup>2</sup> s<sup>-1</sup>) are the liquid water density, water vapor density, water liquid effective diffusivity, and vapor effective diffusivity, respectively;  $S_{lq}$  and  $S_{ice}$  represent the local volume fraction of liquid water and ice in the pores, respectively, and  $c_{vap}$  (mol m<sup>-3</sup>) is the vapor mole concentration;  $S_{vap}$  (kg m<sup>-3</sup> s<sup>-1</sup>) is the mass source term of vapor.

As for ice, the mass conservation equation is as follows,

$$\frac{\partial(\varepsilon\rho_{ice}S_{ice})}{\partial t} = S_{ice}$$

where  $\rho_{ice}$  (kg m<sup>-3</sup>) is the ice density, and  $S_{ice}$  (kg m<sup>-3</sup> s<sup>-1</sup>) is the mass source term of ice.

The source terms of the above governing equations are shown in Table 3. The source terms ( $S_{i,j}$ ) from water phase  $i$  to water phase  $j$  are listed in Table 4.

When generated by an electrochemical reaction, the water molecular will immigrate from anode electrolyte to cathode electrolyte by combining with the hydrogen ion (called electro-osmosis process). The process becomes more obvious as the current increases [42]. Therefore, the electro-osmosis drag source term  $S_{EOD}$  is considered in the numerical model, and it can be calculated by

$$S_{EOD} = \nabla \cdot \left( \frac{n_d}{F} \kappa_{ion}^{eff} \nabla \phi_{ion} \right) \quad (9)$$

where  $n_d$  is the electro-osmotic drag coefficient and related closely to the membrane water content:

**Table 3**  
Source terms of mass conservation equations.

Terms	Expression	Unit
Non-frozen membrane water	$S_{nfm} =$	kmol m <sup>-3</sup> s <sup>-1</sup>
Frozen membrane water	$S_{fm} = S_{n-f} - S_{n-i} + S_{EOD}$ (in membrane)	kmol m <sup>-3</sup> s <sup>-1</sup>
Liquid water	$S_{lq} = S_{i-l} + S_{n-l}M_{H_2O}$	kg m <sup>-3</sup> s <sup>-1</sup>
Water vapor	$S_{vp} = \begin{cases} -S_{v-i} + S_{n-v}M_{H_2O} & (\text{in CL}) \\ -S_{v-i} & (\text{in GDL and MPL}) \end{cases}$	kg m <sup>-3</sup> s <sup>-1</sup>
Ice	$S_{ice} = \begin{cases} S_{v-i} - S_{i-l} + S_{n-l}M_{H_2O} & (\text{in CL}) \\ S_{v-i} - S_{i-l} & (\text{in GDL and MPL}) \end{cases}$	kg m <sup>-3</sup> s <sup>-1</sup>

**Table 4**  
Phase change source terms of water transition [43].

Terms	Expression	Unit
Non-frozen membrane water – frozen membrane water	$S_{n-f} = \begin{cases} \frac{\xi_{n-f} \rho_{mem}}{EW} (\lambda_{nfm} - \lambda_{sat}) & (\text{if } \lambda_{nfm} > \lambda_{sat}) \\ \frac{\xi_{n-f} \rho_{mem}}{EW} \lambda_{nfm} & (\text{if } \lambda_{nfm} < \lambda_{sat}) \end{cases}$	$\text{mol m}^{-3} \text{s}^{-1}$
Non-frozen membrane water – water vapor	$S_{n-v} = \frac{\xi_{n-v} \rho_{mem}}{EW} (\lambda_{nfm} - \lambda_{equil})(1 - s_{li} - s_{ice})$	$\text{mol m}^{-3} \text{s}^{-1}$
Non-frozen membrane water – ice	$S_{n-i} = \begin{cases} \frac{\xi_{n-i} \rho_{mem}}{EW} (\lambda_{nfm} - \lambda_{sat})(1 - s_{li} - s_{ice}) & (\text{if } \lambda_{nfm} > \lambda_{sat}) \\ 0 & (\text{if } \lambda_{nfm} < \lambda_{sat}) \end{cases}$	$\text{kg m}^{-3} \text{s}^{-1}$
Ice-liquid water	$S_{i-l} = -\xi_{i-l} \varepsilon s_{ice} \rho_{ice} \quad (\text{if } T \geq T_N)$	$\text{kg m}^{-3} \text{s}^{-1}$
Water vapor-ice	$S_{v-i} = \begin{cases} \xi_{v-i} \varepsilon (1 - s_{li} - s_{ice}) \frac{(p_g X_{vp} - p_{sat}) M_{H_2O}}{RT} & (\text{if } p_g X_{vp} \geq p_{sat}) \\ 0 & (\text{if } p_g X_{vp} < p_{sat}) \\ 0 & (\text{if } T \geq T_N) \end{cases}$	$\text{kg m}^{-3} \text{s}^{-1}$

**Table 5**  
Voltage loss of the PEMFC cell.

Voltage loss	Analytical Equation	Unit
Activation voltage loss	$V_{act} = \frac{RT}{\alpha F} \ln \left( \frac{I}{(1 - s_{ice} - s_{li})^{0.5} j \cdot \delta_{CL} \left( \frac{0.21 \cdot p_c \cdot (1 + (1 - 1/\xi))}{2RT \cdot c_{ref}} \right)} \right)$	V
Concentration voltage loss	$V_{conc} = \frac{RT}{\alpha F} \ln \left( 1 - \frac{I}{j_D} \right)$	V
Ohmic voltage loss	$V_{ohmic} = -ASR \cdot j$	V

$$n_d = \frac{2.5 \lambda_{nfm}}{22} \quad (10)$$

### 2.2.2. Heat transport

The energy conservation equation is expressed as

$$\frac{\partial}{\partial t} \left( (\rho c_p)_{fl,sl}^{eff} T \right) = \frac{\partial^2 (k_{fl,sl}^{eff} T)}{\partial x^2} + S_T \quad (11)$$

where  $(\rho c_p)_{fl,sl}^{eff}$  and  $k_{fl,sl}^{eff}$  denote the effective heat capacity ( $\text{J kg}^{-1} \text{K}^{-1}$ ) and effective thermal conductivity ( $\text{W m}^{-1} \text{K}^{-1}$ ), respectively, as shown in Table 2;  $S_T$  ( $\text{W m}^{-3}$ ) represents the thermal source term, which includes the reversible heat, the activation heat, ohmic heat, and latent heat. The source term of different cell assembly components is expressed as

$$S_T = \begin{cases} j_c \eta_{act} + \frac{I^2 ASR_{CL}}{3 \delta_{CL}} + S_{PC} & (\text{in anode CL}) \\ \frac{j_c T \Delta S}{2F} + j_c \eta_{act} + \frac{I^2 ASR_{CL}}{3 \delta_{CL}} + S_{PC} & (\text{in cathode CL}) \\ \frac{I^2 ASR_{GDL}}{\delta_{GDL}} + S_{PC} & (\text{in GDL}) \\ \frac{I^2 ASR_{BP}}{\delta_{BP}} & (\text{in BP}) \\ \frac{I^2 ASR_{mem}}{\delta_{mem}} + S_{PC} & (\text{in membrane}) \end{cases} \quad (12)$$

where  $ASR_i$  ( $\Omega \text{ m}^{-2}$ ) is the area-specific resistance,  $\eta_{act}$  (V) is the activation over-potential, and  $j_c$  ( $\text{A m}^{-3}$ ) is the reaction rate.

### 2.2.3. The output performance of the stack

The main voltage drops of the cell are caused by the activation voltage loss ( $V_{act}$ , V), concentration voltage loss ( $V_{conc}$ , V), and ohmic voltage loss ( $V_{ohmic}$ , V). The output voltage of the PEMFC is solved by Equation (13).

$$V_{out} = V_{nernst} + V_{act} + V_{conc} + V_{ohmic} \quad (13)$$

The first term on the right side of the above equation is Nernst voltage, also known as the open-circuit voltage. And it is expressed as

$$V_{nernst} = 1.23 - 0.9 \times 10^{-3} \cdot (T - T_0) + \frac{RT_0}{2F} \ln \left( \frac{p_{H_2} \cdot p_{O_2}}{p_{H_2O}} \right) \quad (14)$$

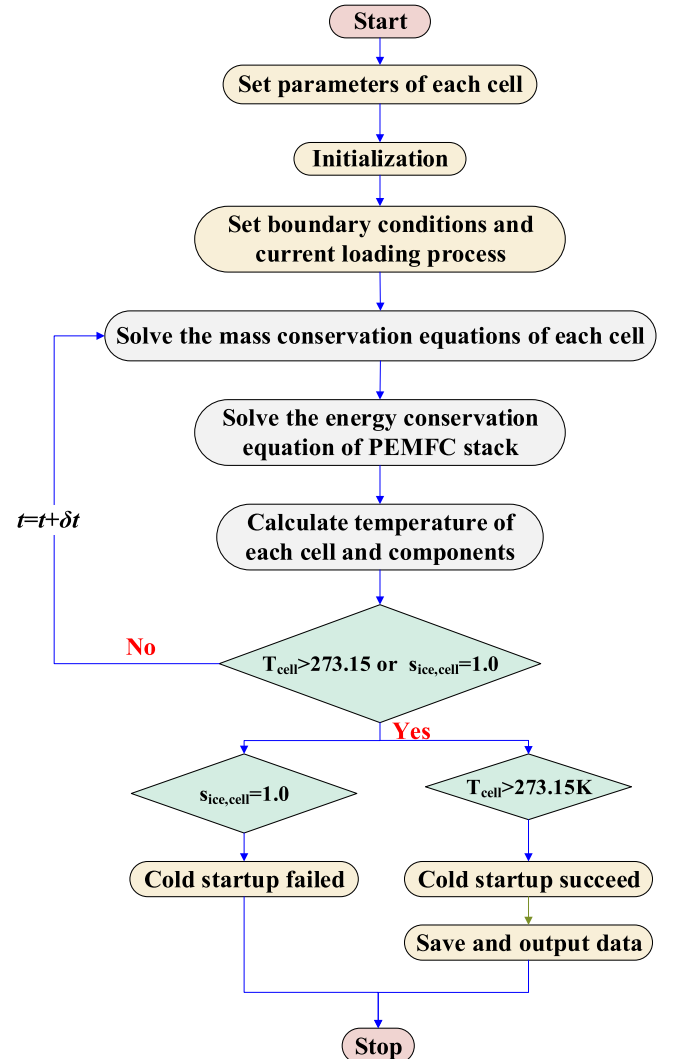
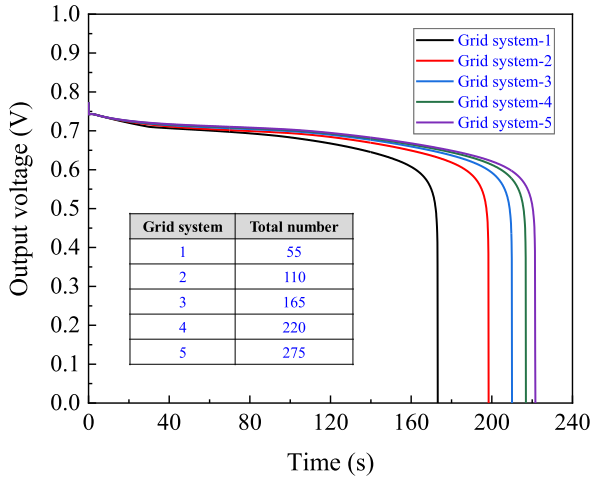
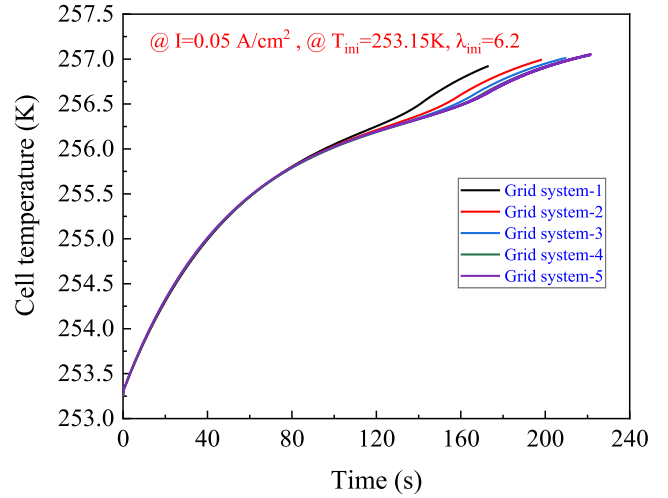


**Fig. 4.** Numerical simulation procedure of the present model.



(a) Output voltage



(b) Cell temperature

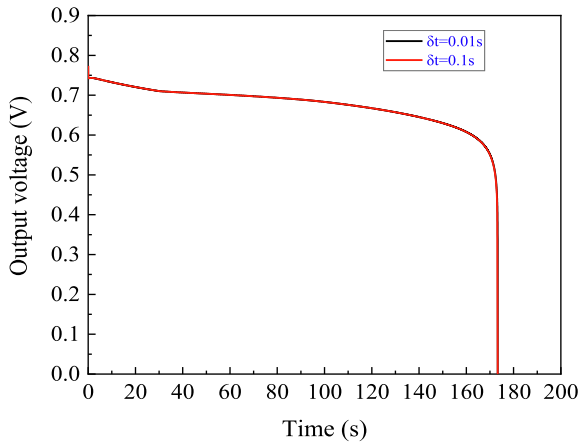
Fig. 5. Grid system independence test.

where  $T_0$  is a constant temperature (298.15 K);  $p_{H_2}$ ,  $p_{O_2}$  and  $p_{H_2O}$  are the partial pressure of different gas species  $H_2$ ,  $O_2$ , and  $H_2O$  (g), respectively. The equations for determining the rest three terms are shown in Table 5. In the present model, the Tafel equation [44] is adopted to analytically calculate the activation loss [13,16,22,28,36]. It should be noted that the exchange current density of electrochemical reaction is corrected by the volume fraction of ice and water liquid, also related closely to the stoichiometric ratio. And  $j_D$  in the concentration voltage loss equation is defined as

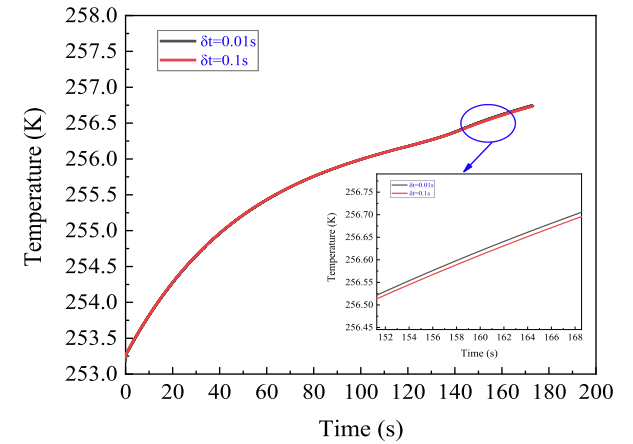
$$j_D = \frac{4F \cdot c_h}{\frac{\delta_{GDL}}{D_{GDL}^{eff}} + \frac{\delta_{MPL}}{D_{MPL}^{eff}} + 0.5 \frac{\delta_{CL}}{D_{CL}^{eff}}} \quad (15)$$

where  $D_{GDL}^{eff}$ ,  $D_{MPL}^{eff}$  and  $D_{CL}^{eff}$  are effective diffusivity of water vapor inside the GDL, MPL, and CL, respectively. The total area-specific resistance ASR ( $\Omega$ ) is calculated by Eq. (16), where  $\sigma_i$  denotes the electric conductivity.

$$ASR = A_{cell} \left( \frac{\delta_{BP}}{\sigma_{BP} A_{cell}} + \frac{\delta_{GDL}}{\sigma_{GDL} A_{cell}} + \frac{\delta_{MPL}}{\sigma_{MPL} A_{cell}} + \frac{\delta_{CL}}{\sigma_{CL} A_{cell}} + \frac{\delta_{mem}}{\sigma_{mem} A_{cell}} \right) \quad (16)$$



(c) Output voltage



(d) Cell temperature

Fig. 6. Time step independence test.

As for the PEMFC stack, the mean output voltage and power are determined by Eqs. (17) and (18), respectively. In Eq. (18), the current changes with time ( $t$ ) according to the current loading method.

$$V_{stack} = \sum_{i=1}^{n_{cell}} V_{out,i} \quad (17)$$

$$P_{stack} = I(t) \cdot \sum_{i=1}^{n_{cell}} V_{out,i} \quad (18)$$

### 2.3. Boundary and initial conditions

The heat loss from the two end surfaces by the convective heat transfer process mentioned above is expressed as

$$Q_{loss} = h A_{cell} (T_{sur} - T_{wall}) \quad (19)$$

where  $h$  ( $W m^{-2} K^{-1}$ ) represents the heat transfer coefficient,  $T_{sur}$  (K) is the ambient temperature.  $T_{wall}$  (K) is the temperature of the endplate surface, which is replaced by the average temperature of BPs in this study.

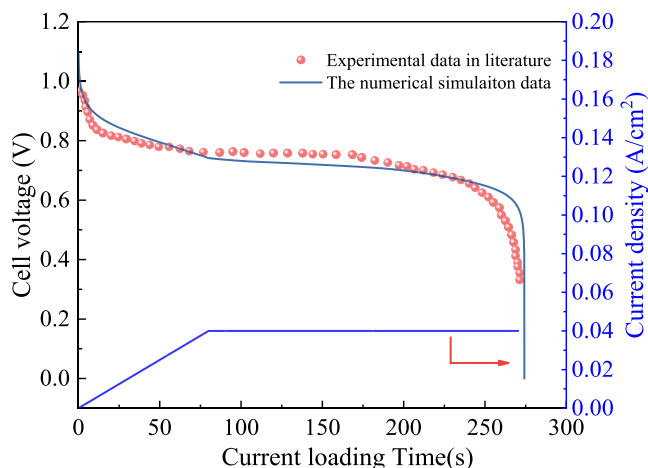


Fig. 7. Comparison of results between the present simulation and experiment data in reference [45].

The initial temperature is set as 253.15 K in each cell. The initial membrane water content is set as 6.2 [45]. The current is defined by the specified loading process.

It is to be noted here that simulating a stack with more than ten cells only adds the simulation region and the simulation time but does not affect the simulation approach and the numerical accuracy.

#### 2.4. Numerical simulation procedure

The numerical simulation of the PEMFC stack cold start-up process is conducted by self-programming code based on the commercial software MATLAB. The details of the simulation procedure are shown in Fig. 4. In the beginning, the parameters of every single-cell and each component are defined and initialized. After that, the current loading process is implemented. At every time step, the mass governing equations of five kinds of water are solved in each single-cell. After the concentration distributions, volume fractions, and mass source terms of different water phases are obtained, energy source terms can be calculated according to the source term equations. Subsequently, the energy conservation equation is solved in the entire simulated stack region. And the temperature distribution of the stack among the through-plane direction can be achieved. The fourth-order Runge-Kutta method [13,28] is used to solve the discretized governing equations.

For the cold start-up process, in Ref. [28], the average ice volume fraction of the stack is used as the criterion for determining whether it is successful or not. In this way, the cell voltage would be zero during a period, but such a phenomenon is not allowed in an actual PEMFC stack running. In the present study, the specific criteria for a successful cold start-up are set as follows: the maximum ice volume fraction of CLC should be less than 1, and the cell temperature is larger than 273.15 K in every cell. And the voltage of every single cell must be above 0 V during the entire cold start-up process. If the cell temperature is greater than 273.15 K, the cold start-up can be considered to be successful, otherwise continuing the above solving procedure at the next time step. When the monitored ice volume fraction of ice reaches to 1, the start-up process is failed, and the simulation procedure is stopped.

### 3. Model validation

#### 3.1. Grid system independence test

A proper grid system needs to be chosen to balance the accuracy and efficiency of the numerical simulation. A single cell with a current density of  $0.05 \text{ A cm}^{-2}$  is taken as the representative to test the grid independence. The temperature and output cell voltage variation trends

for five grid systems are shown in Fig. 5. As the total grid number is growing, the difference in temperature and output voltage, compared with the former grid system, is tending to be smaller. To be time-efficiency, the grid system-3 is used to conduct the subsequent study, and the final grid number of the MEM, CL, MPL, GDL, CH, and BP are 25, 20, 20, 20, 5, 5, respectively.

Fig. 6 illustrates the results of time step independence tests. The output voltage and temperature show no noticeable difference under the two adopted values (0.1 s and 0.01 s). Considering that the current loading process must have a comparatively small time step, the final step is set as 0.01 s in all cases.

#### 3.2. Model validation

The one-dimensional numerical model was validated by comparing the cell output voltage with the experimental data in Ref [45] during the cold start-up process from  $-20 \text{ }^\circ\text{C}$ . The loading current density takes a ramp of  $0.5 \text{ mA cm}^{-2} \text{ s}^{-1}$  for the first 80 s and then keeps a constant of  $40 \text{ mA cm}^{-2}$  until the cold start-up process is finished. The two results are compared in Fig. 7. It can be found that most numerical results are in good agreement with the experimental data during the loading stage, showing the reliability of the present model and the developed code. It is interesting to note that some appreciable deviation occurs at the shut-down stage (after 225 s). To the authors' knowledge, it is a common situation between numerical simulation and test data for cold-startup of PEMFC [28,35,36].

### 4. Five current loading modes

This section introduces five different current loading modes, and the requirements for a successive cold start-up process are presented. According to the above model validated section, a maximum current of 1.0 A leads to a fail-down of the cold start-up. To obtain a successful cold start-up, we enlarge the maximum current to 1.25 A for the current loading modes.

#### 4.1. Description of the current loading modes

##### 4.1.1. Constant current loading mode

Constant current mode is a common way of PEMFC cold start-up in the literature [13]. This paper considers the constant current mode a primary case for the comparative analysis of different cold start-up modes. The selected constant current is 1.25 A.

##### 4.1.2. Constant slope current ramp mode

Ramp loading mode is one of the most common modes applied in the cold start-up [46]. At the beginning stage, a lower current ramp value can keep the loading, and the start-up process continues. The slope is an essential parameter in this mode. A too-large slope will cause a rapid increase of the current, and then the stack voltage will decrease quickly, leading to the shut-down of a stack. Therefore a suitable loading slope must be selected before using the current loading mode.

For the constant slope mode, the electrical current is calculated by Eq. (20).

$$I = \alpha \cdot t \quad (20)$$

where  $\alpha$  represents the ramp slope and equals  $12.5 \text{ mA s}^{-1}$  in the present study.

##### 4.1.3. Variable slope current ramp mode

An improved current ramp mode with changing slope determined by a specified output voltage (threshold) is studied. A larger slope is used in this mode when the voltage is higher than the specified value, and a smaller slope is adopted when the voltage is less than it. Several thresholds can be specified to have a more accurate and timely control

**Table 6**  
Detailed parameters of five current loading modes.

Cases	Ramp slope/ mA s <sup>-1</sup>	Loading cycle/s	Waiting time	Voltage threshold/V	Maximum current/A
Case-1	-	-	-	-	1.25
Case-2	$\alpha = 12.5$	-	-	-	1.25
Case-3	$\alpha_1 = 12.5$ $\alpha_2 = 8.0$	-	-	0.4	1.25
Case-4	$\beta_1 = 10$ $\beta_2 = 2$	2.5	-	-	1.25
Case-5	$\alpha = 60.0$	1.75	0.3	0.15	1.25

process of the stack start-up. One threshold is used in the present work for this mode, and the current is loaded according to Equation (21).

$$I = \begin{cases} I + \alpha_1 \cdot \delta t & (\text{if } V_{out,cell} \geq V_{threshold}) \\ I + \alpha_2 \cdot \delta t & (\text{if } V_{out,cell} < V_{threshold}) \end{cases} \quad (21)$$

where  $\alpha_1$  and  $\alpha_2$  are equal to 12.5 mA s<sup>-1</sup> and 8.0 mA s<sup>-1</sup>, respectively, and the threshold voltage is set as 0.4 V.

#### 4.1.4. Zigzag current loading mode

As described in Ref. [19], zigzag loading mode adopts an alternatively increasing and decreasing current density with time to reduce the start-up time. In this mode, the current density changes by a zigzag way. Precisely, in the present paper, the current is calculated by following piecewise function

$$I = \begin{cases} I + \beta_1 \cdot \delta t & (\text{if } 0.0 < t_{load} \leq \frac{1}{2} t_{cycle}) \\ I - \beta_2 \cdot \delta t & (\text{if } \frac{1}{2} t_{cycle} < t_{load} \leq t_{cycle}) \end{cases} \quad (22)$$

where  $\beta_1$  and  $\beta_2$  represent the current increase slop and decrease slop, respectively,  $\delta t$  (s) is the time step,  $t_{cycle}$  is the time period of each loading cycle, and  $t_{load}$  is the total loading time. In this study,  $\beta_1$ ,  $\beta_2$ ,  $t_{cycle}$  are 10 mA s<sup>-1</sup>, 2 mA s<sup>-1</sup>, and 2.5 s, respectively.  $t_{load}$  is expressed as

$$t_{load} = t - \text{mod} \left( \frac{t}{t_{cycle}} \right) \cdot t_{cycle} \quad (23)$$

#### 4.1.5. Stepwise-changed current loading mode

In this mode, the loading current changes stepwisely. To realize this mode, a relatively large ramp slope is adopted in a short loading cycle, making the start-up process produce little water while the temperature can rise. Once the current reaches a certain value, a waiting time is set to keep the current constant after a ramp stage in one loading cycle. In this study, the current of the loading process is expressed as Eq. (24). It can be seen that the current loading slope is also stepwisely changed according to the output voltage.

$$\begin{cases} \begin{cases} I = I_0 + \alpha \cdot \delta t & \text{if } (0.0 < t_{load} \leq 0.1 t_{cycle}) \\ I = I & \text{if } (0.1 t_{cycle} < t_{load} \leq t_{cycle}) \end{cases} & \text{if } (V_{out,cell} > 0.3) \\ \begin{cases} I = I_0 + \frac{1}{3} \alpha \cdot \delta t & \text{if } (0.0 < t_{load} \leq 0.1 t_{cycle}) \\ I = I & \text{if } (0.1 t_{cycle} < t_{load} \leq t_{cycle}) \end{cases} & \text{if } (0.15 < V_{out,cell} \leq 0.3) \\ I = I - 0.05 & \text{if } (V_{out,cell} \leq 0.15) \end{cases} \quad (24)$$

where  $\alpha$  (A s<sup>-1</sup>) is the loading slope and set as 60 in the following study, and  $t_{cycle}$  is the current loading cycle in the process.

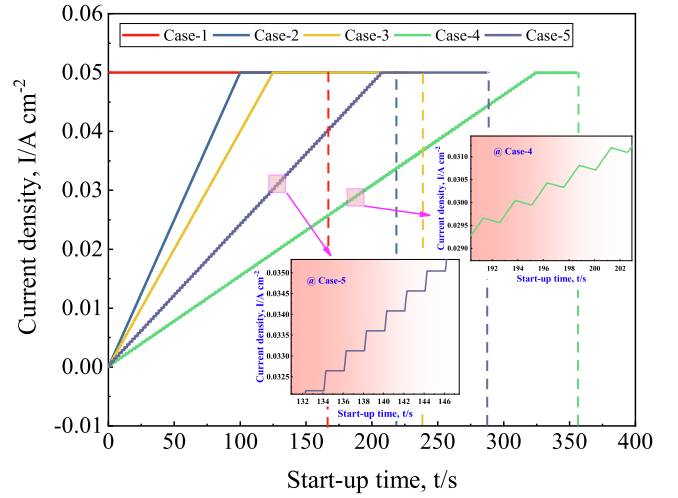


**Fig. 8.** Current density variation of the five cases.

## 4.2. Requirements for a successful cold start-up

The quantity of heat generation ( $Q_{Heat}$ , the unit is J cm<sup>-2</sup>) and the amount of product water ( $m_{H_2O}$ , mg cm<sup>-2</sup>) [33] are two important characteristic parameters that can be calculated by Eqs. (25) and (26), respectively.

$$Q_{Heat} = \int (E_h - V_{cell}) I dt \approx (E_h - V_{cell}) \int I dt \quad (25)$$

$$m_{H_2O} = \frac{M_{H_2O}}{2F} \int I dt \quad (26)$$

where  $E_h$  represents the ideal thermal potential (1.48 V for the H<sub>2</sub>-O<sub>2</sub> reaction), and  $M_{H_2O}$  (g mol<sup>-1</sup>) is the molecular weight of water.

For a successful cold start-up process of the PEMFC stack, keeping a higher heat generation rate and a relatively lower water production rate is necessary. Therefore, the heat generation rate and water production rate are regarded as the requirements of the cold start-up process.

## 5. Results and analysis

Five simulation cases are designed to study the output performance of the PEMFC stack specified in Section 2 during the cold start-up process by adopting the above five current loading modes, respectively. The detailed information of the five cases is shown in Table 6. To save the simulation time and ensure that the stack will not be shut down in a short period, the maximum current is set to 1.25 A. The other parameters of each case (mode) were determined from our preliminary simulations. An optimal mode can be found for the five specific current loading modes by comparing the heat generation and water production rates. As far as each mode is concerned, their optimal parameter selection is not the focus of the present paper and will be examined in our further research.

During the simulation process, several important dynamic outputting parameters are monitored to show the process characteristics variation.

For the cold start-up process, the essential dynamic features of the PEMFC stack are the variation of the stack temperature, ice volume fraction, and the output voltage changing with the current loading process. The predicted results of cold start-up processes with different current loading modes show that the one-dimensional numerical model could represent and describe the dynamic characteristics clearly and timely. And the predicted output performance of the cold start-up processes is indeed affected by the current loading modes. These results are provided in detail in the following presentation.

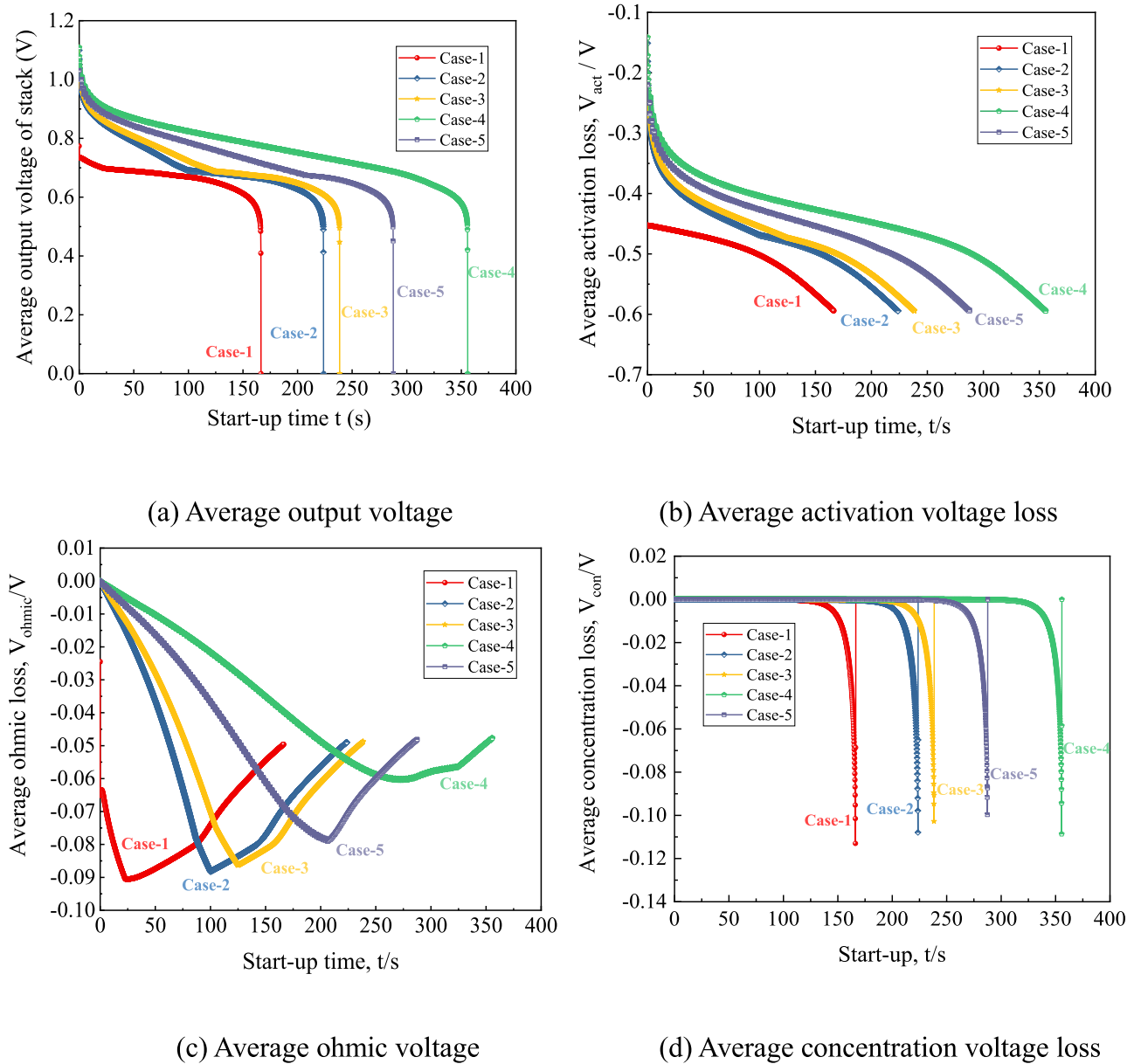


Fig. 9. Output performance of the PEMFC stack.

The following results will be presented and compared in four parts: the output voltage and power, the water content and ice volume fraction, the temperature and ohmic resistance, and the generated heat and produced water.

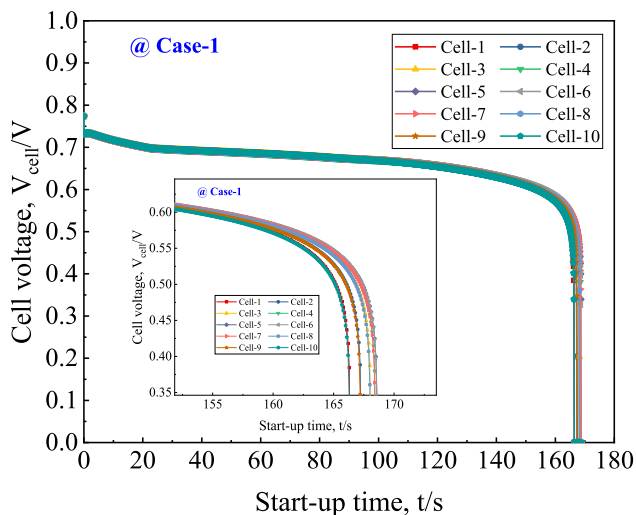
### 5.1. The output voltage and power of the PEMFC stack

Fig. 8 shows the current density variation during the cold start-up of the five simulation cases. According to the criteria set in Section 2.4, the five modes cannot get a successful start-up for the specific situation studied. However, analyzing the output dynamic characteristics of the five cases can reveal the differences between them and help us to find a mode that can meet the requirements for cold start up process and may be recommended for other PEMFC stack running situations, such as a lower temperature than  $-20\text{ }^{\circ}\text{C}$  and more cells for a larger stack. In addition, detailed analyses of the failed start-up process may help us understand the shut-down mechanism and get some valuable hints for a successful cold start-up operation.

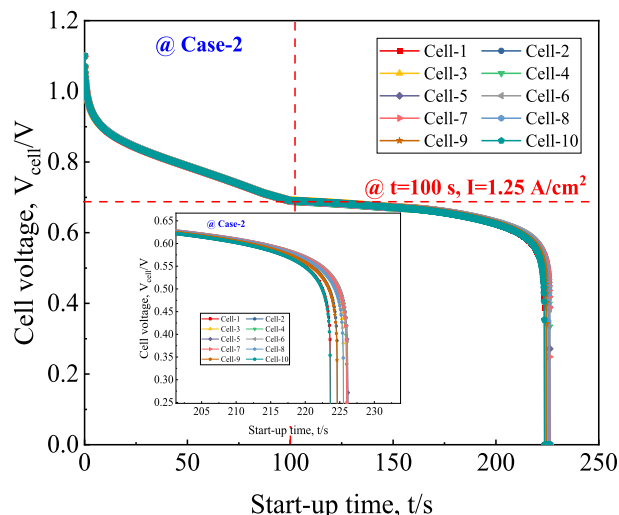
The cold start-up operation time is defined as the time period from

the very beginning to the time of shut-down. The times of the five simulation cases are 166.4, 223.7, 238.5, 355.8, and 287.6 s, respectively. In addition, the time in which the current increases to the maximum for Cases 2, 3, 4, and 5 is 100, 125, 325.4, and 208.2 s, respectively. It can be found that Case-4 has the longest loading time, while Case-1 obtains the shortest start-up operation time. For Case 3 during the operation time period, the output voltage did not meet the condition shown in Eq. (21). Hence only the slope  $\alpha_1$  was used, making the current change linearly with time.

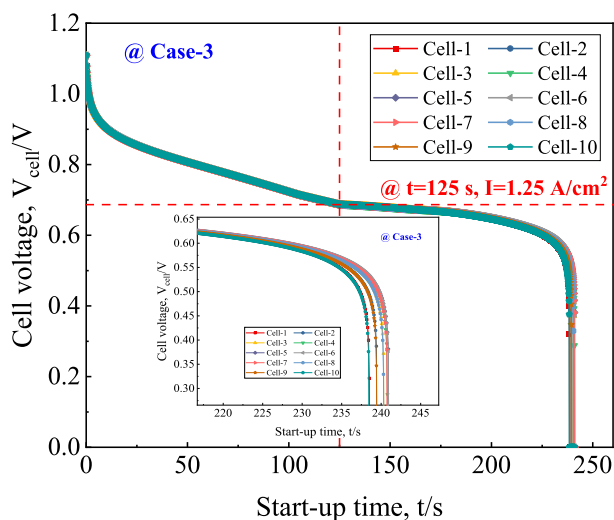
The average voltage and voltage losses are essential dynamic characteristics of the start-up operation. The voltage losses contain the activation voltage loss ( $V_{act}$ , V), ohmic voltage loss ( $V_{ohmic}$ , V), and concentration voltage loss ( $V_{conc}$ , V). Fig. 9(a) shows the variation of the stack output voltage during the cold start-up operation. As can be seen, because having the maximum current value initially, Case-1 gets the smallest output voltage and then gradually decreases during the start-up process. The other cases have a relatively higher voltage due to the current rising from zero gradually. And then, the output voltage of the other four start-up cases decreases quickly because they have a specified



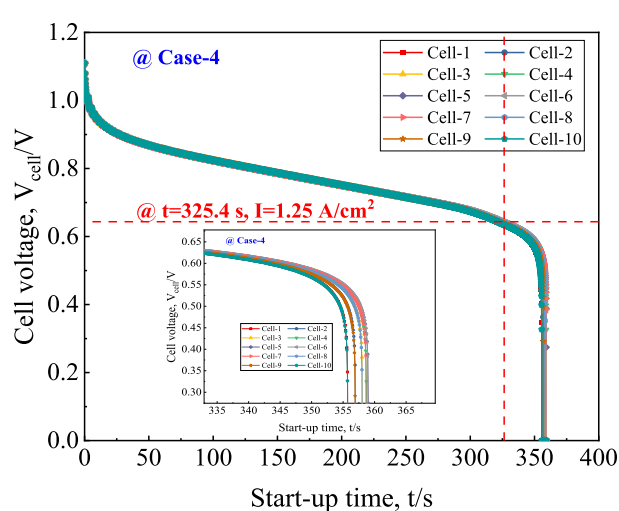
(a) Case 1



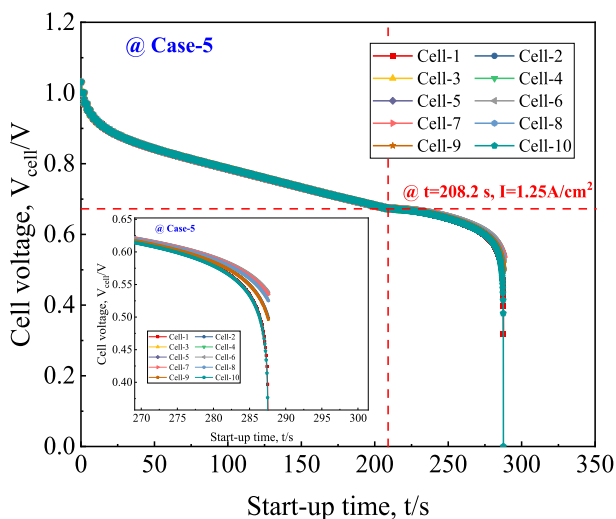
(b) Case 2



(c) Case 3



(d) Case 4



(e) Case 5

Fig. 10. Cell voltage variation under different current loading mode.

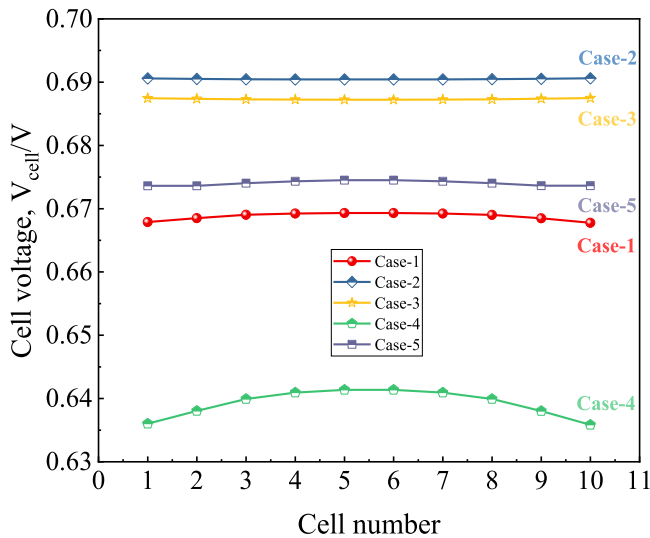


Fig. 11. Cell voltage distribution along the x-direction.

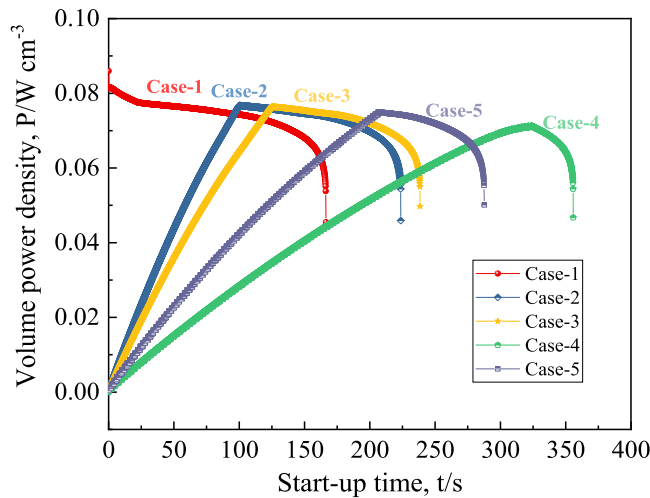


Fig. 12. Variation of volume power density under different cold start-up simulation cases.

ramping slop to raise the current. Among them, the voltage reductions of Case-2 and Case-3 are more than that of Case-4 and Case-5. Fig. 9(b), (c), and (d) show the variation of the average activation voltage loss, average ohmic voltage loss, and average concentration voltage, respectively. We can find that the activation voltage occupies a large proportion in the voltage drop compared with the ohmic and

concentration voltage losses. As the current increases, the ohmic loss is increasing quickly firstly and then decreasing. The concentration voltage loss is mainly related to the ice volume fraction. When the pores of the porous zone are nearly filled by ice, the concentration voltage loss will increase sharply at the shut-down stage.

Fig. 10 gives the real-time voltage variation of the ten cells during the cold start-up of the five cases, where the voltage is recorded when the cell current reaches the maximum current value of  $1.25 \text{ A cm}^{-2}$ . It can be seen that the ten cells in the stack almost have the same output voltage at different time instants. However, from the enlarged figures shown in the left-bottom place of each figure, we can find some differences: the two side cells (Cell-1 and Cell-10) of the stack have a smaller output voltage due to lower cell temperature than that of the middle cells. This variation pattern can be observed clearly in Fig. 11, where voltage variation along the x-direction is presented.

Another essential dynamic output parameter of the PEMFC stack is the volume power density ( $P, \text{ W cm}^{-3}$ ). Fig. 12 shows the variation of the volume power density during the start-up operation. We can find that Case-1 has the largest power density at the beginning stage and then decreases with the reducing output voltage. On the contrary, the other four cases have an increasing trend starting from zero at the initial stage. When the current rises to the maximum value, the volume power density begins to decrease slightly. As the voltage drops quickly, the power density also reduces sharply.

### 5.2. The water content and ice volume fraction

The membrane water content ( $\lambda_{mf}$ ) is a critical intermediate parameter, and it changes with the current. Many physical variables are related to it, such as the effective membrane water diffusion coefficient [47]. Fig. 13 illustrates non-frozen water content variation trends in the representative regions during the cold start-up for the five simulation cases. The water content changes show a similar tendency in the same region, but there is a significant difference between different cases at the same time step. As shown in Fig. 13(a), at the beginning stage, the water content of the membrane water in the cathode catalyst layer begins to increase rapidly with the current loading, and the increasing rate of Case-1 is larger than the others due to the largest current value in a whole cold start-up process. As mentioned in the second section, when the water content is greater than the saturated water content, the ice would produce inside the pores of catalyst layers. Therefore, the water content increasing rate is changing to be slower.

Fig. 13(b) shows the non-frozen water content variation in the anode catalyst layer. Contrary to the changing trend in the cathode catalyst layer, in the beginning, the water content decreases quickly due to the role of the electro-osmotic drag process. When the water content reaches the minimum value, it increases due to the back diffusion process. Fig. 13(c) gives the water content changing trend in the membrane, and there is also a minimum during the entire cold start-up process. It is roughly the same as the changing trend of the anode catalyst layer. The

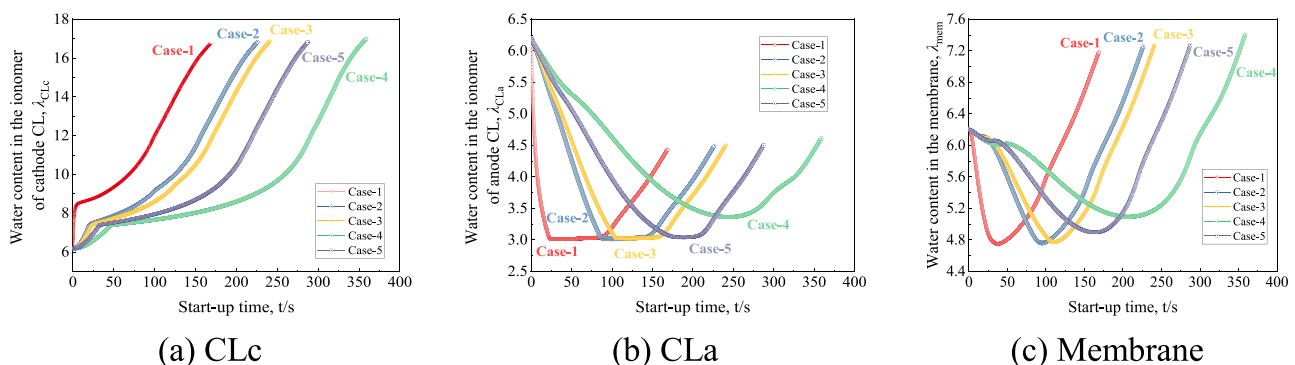


Fig. 13. Variation of water content with the start-up time under different current loading modes.

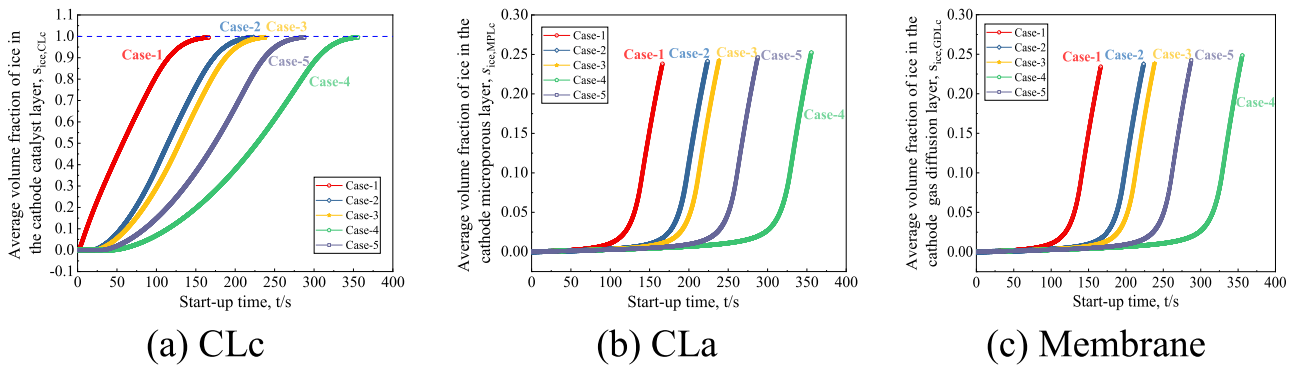


Fig. 14. Average volume fraction of ice.

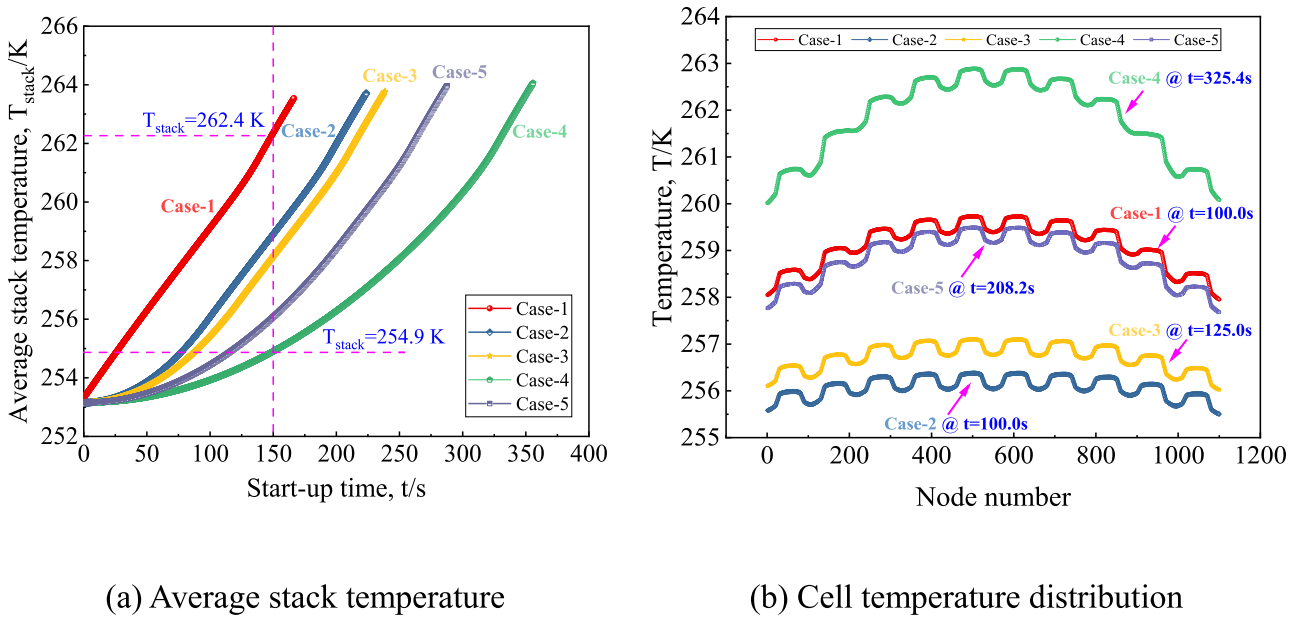


Fig. 15. Temperature of the stack and cells during the current loading process.

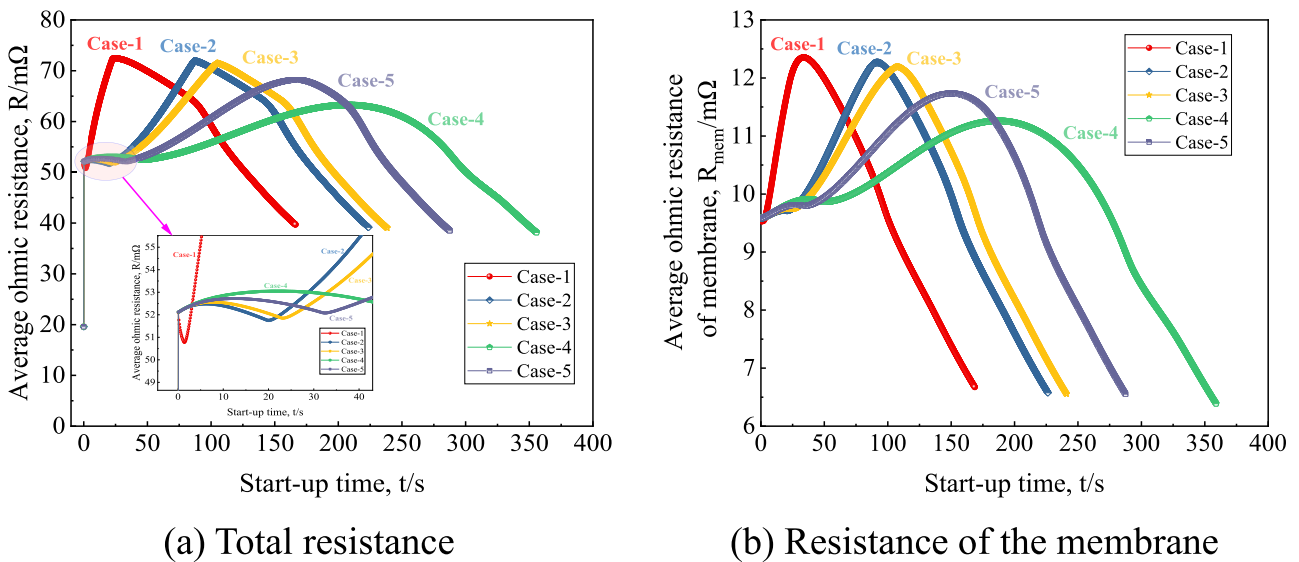
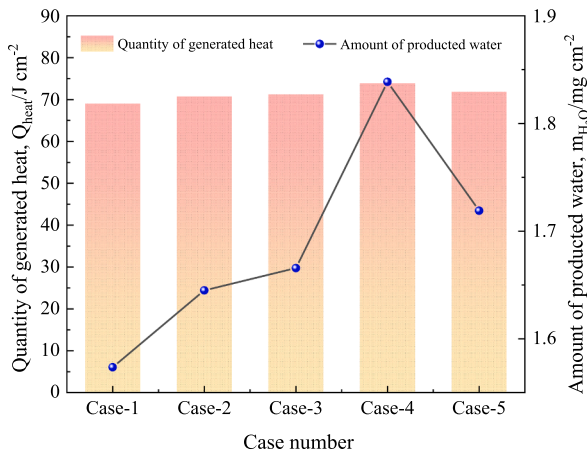
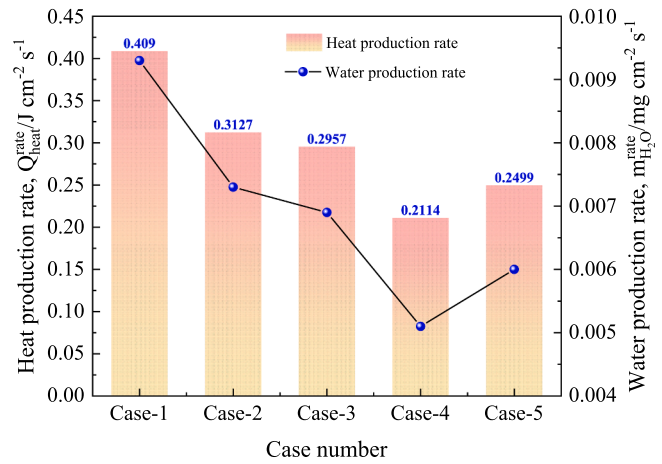


Fig. 16. Average ohmic resistance.



(a) Generated heat and water



(b) Heat and water production rate

Fig. 17. Variation of the evaluation criteria under different simulation cases.

membrane water content firstly decreased and then increased under the roles of the electro-osmotic drag process and back diffusion process. The transform between the non-frozen membrane and frozen membrane water also helps to reduce water content in the membrane.

The volume fraction of ice variation with the start-up time under different current loading modes is plotted in Fig. 14. We can find that the cathode catalyst layer has a much higher ice volume fraction; hence the primary freezing process occurs in this component. Since the diffusion coefficient is relatively low at subzero temperatures, the amount of water vapor in the MPLC and GDLc diffused from the cathode catalyst layer is minimal. Then the ice volume fraction transformed from diffused water vapor is also tiny. Nevertheless, the existence of the MPLC helps to reduce the quantity of ice production in the CLc due to the fact that pore volume provides the space for ice which is transferred from water vapor and makes the start-up process continue. It is easy to see that Case-1 has the fastest ice production rate while Case-5 has the lowest.

Regarding membrane water content and ice quantity, the constant current loading mode (Case-1) is not proper for the PEMFC cold start-up process because of the fast ice production rate in pores, while Case-4 and Case-5 are better to balance the water content and ice volume fraction.

5.3. The temperature and ohmic resistance

The stack (or cell) temperature is a vital monitoring parameter in a cold start-up process. Fig. 15(a) shows the real-time temperature variation of the PEMFC stack. As can be seen, the stack temperature rises quickly in Case-1 initially. However, in other cases, the temperature is increasing gradually with Case-4 having the lowest temperature. At time = 100 s, the average stack temperature difference between the five cases is about 7 °C. Fig. 15(b) shows the cell temperature distribution along the x-direction during the cold start-up process (except Case-1, the

time of data statistics is the time to reach the maximum current). It is evident that the cells at both sides of the PEMFC stack have a lower temperature than the middle cells since the convective heat transfers with the cold environment. Because of the longer loading time, the cell temperature in Case-4 is higher than in other cases.

A proper temperature rising rate is needed for the cold start-up process to keep a shorter start-up time and a smaller ohmic voltage loss. Thus, Case-2, Case-3, and Case-5 are better than others.

The ohmic heat source is a significant one at the initial start-up process, closely related to the ohmic inner resistance of the cell components and loading current. Fig. 16 shows the variation of averaged ohmic resistance of the stack and the membrane.

At the initial time, the ohmic resistance is 20 mΩ calculated according to the initial water content and temperature, and when the current is applied, the resistance begins to rise. It can be seen that Case-1 gains a fastly growing rate, while the other cases have a less and different increasing trend. The water content of Case-1 is quickly increasing (as shown in Fig. 13(a)), leading to a rapid increase of resistance. Because of the largest current at the start time, the electro-osmotic drag process is also more severe to reduce the water content in the CLa (as shown in Fig. 13(b)) and then increase the ohmic resistance. Different from Case-1, the ohmic resistances of the other cases are growing slightly at the beginning stage. Also, the function of the electro-osmotic drag process is weak under a very low current value. Under the combined role of the two weakly processes, the ohmic resistance is also increasing gradually. In all cases, the resistance increase is attributed to the decreasing water content, while the decrease is due to the temperature rising quickly under a relatively high current. It must be stated that the total ohmic resistance of the stack is no more than 70 mΩ, and the ohmic resistance of the membrane is reducing to below 10 mΩ at the shut-down stage.

The ohmic resistance should not be too large to ensure that ohmic

Table 7 Comparisons of five modes.

Terms	Current loading modes				
	Case-1 Constant current	Case-2 Constant slope	Case-3 Variable slope	Case-4 Zigzag	Case-5 Stepwise
Start-up time	Good	Appropriate	Appropriate	inferior	Appropriate
The ice volume fraction in CLc	inferior	Appropriate	Appropriate	Appropriate	Good
Temperature rising rate	Good	Appropriate	Appropriate	inferior	Appropriate
The ohmic resistance	inferior	inferior	inferior	Good	Appropriate
Rate of heat generation	Good	Appropriate	Appropriate	inferior	Appropriate
Rate of water production	inferior	Appropriate	Appropriate	Good	Appropriate

voltage loss is relatively lower at the beginning time of cold start-up. Therefore, Case-1 can not meet the need. Although the ohmic resistance of the stack at the initial stage can be reduced by reducing the current loading value, it will significantly increase the start-up time.

Considering the requirement of temperature rising rate, lower voltage drop, and gradually increasing resistance at the initial stage, the current loading mode of Case-5 is the proper current loading mode.

#### 5.4. The quantity of generated heat and amount of produced water

As claimed before, the quantity of generated heat and the amount of produced water are two important parameters of the cold start-up process. Fig. 17 shows the variation of the two parameters under the five simulation cases. Fig. 17(a) gives the quantity of generated heat and the amount of produced water. It can be found that Case-4 obtains the most significant heat production, also gains the largest water production, while Case-1 has the smallest amount of heat and water.

Since the start-up operation time period is different among the five cases, it is not suitable to use heat generation quantity and water production amount in the whole time period for comparison between different modes, rather the heat generation rate and water production rate should be used. The results are shown in Fig. 17(b). Obviously, Case-1 obtains the largest production rates of heat and water because of the shorter continuing time of the start-up operation process, Case-2 and Case-3 followed, while Case-4 gains the smallest. According to the requirements stated in Section 4-2, Case-5 is the best one among the five cases (modes).

The above comparative studies are summarized in Table 7. The three levels (good, appropriate, and inferior) are used to mark the performance. The start-up time and the ice volume fraction in CLC, temperature rising rate, ohmic resistance, heat generation rate, and water production rate are used as comparison indices. Case-5 (stepwise current loading mode) is the best among the five modes for the PEMFC cold start-up process.

## 6. Conclusions

In the present work, a transient one-dimensional cold start-up model of the PEMFC stack is developed and used to study the effects of current loading modes on the dynamic output characteristics to find an appropriate current loading mode. Five different current loading modes are designed and implemented. There are constant current loading mode, constant slope ramp loading mode, variable slope ramp loading mode, zigzag current loading mode, and stepwise-changed current loading mode. Some conclusions are obtained by monitoring and comparatively analyzing the output voltage, voltage losses, several intermediate parameters, and two requirements. The major findings are as follows:

- (1) The constant current loading mode (used in Case-1) can not fit the requirements of the cold start-up process of the PEMFC stack due to its most significant ice production rate and a higher ohmic resistance caused by a high current value at the beginning stage.
- (2) The ohmic resistance of the PEMFC stack is closely related to the water content and temperature. In the cold start-up process, the ohmic resistance increases firstly and then decreases, finally reaching a minimum value at the end of the process.
- (3) The zigzag current loading mode is unsuitable for the PEMFC cold start-up process due to its longest time and lowest heat generation rate.
- (4) Take the above comparison results and the requirements for cold start-up into account, the stepwise-changed current loading mode (used in Case-5) is the best for the cold start-up process.

#### CRedit authorship contribution statement

Le Lei: Methodology, Software, Data curation, Writing – original

draft, Validation. **Pu He**: Conceptualization, Visualization. **Peng He**: Investigation, Visualization, Supervision. **Wen-Quan Tao**: Conceptualization, Supervision, Writing – review & editing.

#### Declaration of Competing Interest

The authors declare that they have no known competing financial interests or personal relationships that could have appeared to influence the work reported in this paper.

#### Acknowledgment

This work is supported by the key project of NNSFC (51836005), The International Exchange Cooperation Project of NSFC-STINT (51911530157), The National Key Research and Development Program (2017YFB0102702), The Basic research Project of Shaanxi Province (2019ZDXM3-01), and the Foundation for Innovative Research Groups of the National Natural Science Foundation of China (51721004).

#### References

- [1] Cha SW, O'Hayre R, Colella W, Prinz FB. Fuel cell fundamentals. 3rd ed. Canada: Wiley; 2009.
- [2] Wang Y, Chen KS, Mishler J, Cho SC, Adroher XC. A review of polymer electrolyte membrane fuel cells: technology, applications, and needs on fundamental research. *Appl Energy* 2011;88:981–1007.
- [3] Olabi AG, Wilberforce T, Abdelkareem MA. Fuel cell application in the automotive industry and future perspective. *Energy* 2021;214:118955.
- [4] Lü X, Qu Y, Wang Y, Qin C, Liu G. A comprehensive review on hybrid power system for PEMFC-HEV: issues and strategies. *Energy Convers Manage* 2018;171:1273–91.
- [5] Oszcipok M, Riemann D, Kronenwett U, Kreideweis M, Zedda A. Statistic analysis of operational influences on the cold start behaviour of PEM fuel cells. *J Power Sources* 2005;145:407–15.
- [6] Wang Y, Ruiz Diaz DF, Chen KS, Wang Z, Adroher XC. Materials, technological status, and fundamentals of PEM fuel cells – a review. *Mater Today* 2020;32:178–203.
- [7] Amamou AA, Kelouani S, Boulon L, Agbossou K. A comprehensive review of solutions and strategies for cold start of automotive proton exchange membrane fuel cells. *IEEE Access* 2016;4:4989–5002.
- [8] Zhang Q, Tong Z, Tong S, Cheng Z. Research on water and heat management in the cold start process of proton exchange membrane fuel cell with expanded graphite bipolar plate. *Energy Convers Manage* 2021;233:113942.
- [9] Nandy A, Jiang F, Ge S, Wang C-Y, Chen KS. Effect of cathode pore volume on PEM fuel cell cold start. *J Electrochem Soc* 2010;157(5):B726. <https://doi.org/10.1149/1.3355867>.
- [10] Dursch TJ, Trigub GJ, Lujan R, Liu JF, Mukundan R, Radke CJ, et al. Ice-crystallization kinetics in the catalyst layer of a proton-exchange-membrane fuel cell. *J Electrochem Soc* 2014;161(3):F199–207.
- [11] Tabe Y, Yamada K, Ichikawa R, Aoyama Y, Suzuki K, Chikahisa T. Ice formation processes in PEM fuel cell catalyst layers during cold startup analyzed by cryo-SEM. *J Electrochem Soc* 2016;163(10):F1139–45.
- [12] He P, Chen L, Mu YT, Tao WQ. Lattice Boltzmann method simulation of ice melting process in the gas diffusion layer of fuel cell. *Int J Heat Mass Transfer* 2020;149:119121.
- [13] Luo YQ, Jiao K, Jia B. Elucidating the constant power, current and voltage cold start modes of proton exchange membrane fuel cell. *Int J Heat Mass Transfer* 2014;77:489–500.
- [14] Liao ZH, Wei L, Dafalla AM, Suo ZB, Jiang FM. Numerical study of subfreezing temperature cold start of proton exchange membrane fuel cells with zigzag-channeled flow field. *Int J Heat Mass Transfer* 2021;165:120733.
- [15] Yang YB, Ma TC, Du BY, Lin WK, Yao NY. Investigation on the operating conditions of proton exchange membrane fuel cell based on constant voltage cold start mode. *Energies* 2021;14:660.
- [16] Du Q, Jia B, Luo YQ, Chen JX, Zhou YB, Jiao K. Maximum power cold start mode of proton exchange membrane fuel cell. *Int J Hydrogen Energy* 2014;39:8390–400.
- [17] Amamou A, Kandidayeni M, Boulon L, Kelouani S. Real time adaptive efficient cold start strategy for proton exchange membrane fuel cells. *Appl Energy* 2018;216:21–30.
- [18] Amamou A, Boulon L, Kelouani S. An adaptive cold start strategy of proton exchange membrane fuel cell based on maximum power mode. In: 2019 IEEE Vehicle Power and Propulsion Conference (VPPC). IEEE; 2019. p. 1–7.
- [19] Zang L, Hao L. Numerical study of the cold-start process of PEM fuel cells with different current density operating modes. *J Energy Eng* 2020;146:04020057.
- [20] Sun SC, Yu HM, Hou JB, Shao ZG, Yi BL, Ming PW, et al. Catalytic hydrogen/oxygen reaction assisted the proton exchange membrane fuel cell (PEMFC) startup at subzero temperature. *J Power Sources* 2008;177:137–41.

- [21] Guo Q, Luo YQ, Jiao K. Modeling of assisted cold start processes with anode catalytic hydrogen-oxygen reaction in proton exchange membrane fuel cell. *Int J Hydrogen Energy* 2013;38:1004–15.
- [22] Luo YQ, Jia B, Jiao K, Du Q, Yin Y, Wang HZ, et al. Catalytic hydrogen-oxygen reaction in anode and cathode for cold start of proton exchange membrane fuel cell. *Int J Hydrogen Energy* 2015;40:10293–307.
- [23] Jiang W, Song K, Zheng BL, Xu YC, Fang RS. Study on fast cold start-up method of proton exchange membrane fuel cell based on electric heating technology. *Energies* 2020;13:4456.
- [24] Zhan ZG, Yuan C, Hu ZR, Wang H, Sui PC, Djilali N, et al. Experimental study on different preheating methods for the cold-start of PEMFC stacks. *Energy* 2018;162:1029–40.
- [25] Yang Z, Jiao K, Wu K, Shi W, Jiang S, Zhang L, et al. Numerical investigations of assisted heating cold start strategies for proton exchange membrane fuel cell systems. *Energy* 2021;222:119910.
- [26] Khandelwal M, Lee SH, Mench MM. One-dimensional thermal model of cold-start in a polymer electrolyte fuel cell stack. *J Power Sources* 2007;172:816–30.
- [27] Yesilyurt S, Siegel JB, Stefanopoulou AG. Modeling and experiments of voltage transients of polymer electrolyte membrane fuel cells with the dead-ended anode. *J Fuel Cell Sci Technol* 2012;9.
- [28] Zhou YB, Luo YQ, Yu SH, Jiao K. Modeling of cold start processes and performance optimization for proton exchange membrane fuel cell stacks. *J Power Sources* 2014;247:738–48.
- [29] Huo S, Jiao K, Park JW. On the water transport behavior and phase transition mechanisms in cold start operation of PEM fuel cell. *Appl Energy* 2019;233:776–88.
- [30] Ko J, Ju H. Numerical evaluation of a dual-function microporous layer under subzero and normal operating temperatures for use in automotive fuel cells. *Int J Hydrogen Energy* 2014;39:2854–62.
- [31] Wei L, Liao ZH, Suo ZB, Chen XS, Jiang FM. Numerical study of cold start performance of proton exchange membrane fuel cell with coolant circulation. *Int J Hydrogen Energy* 2019;44:22160–72.
- [32] Wang Y, Mishler J. Modeling and analysis of polymer electrolyte fuel cell cold-start; 2010.
- [33] Tajiri K, Tabuchi Y, Wang C-Y. Isothermal cold start of polymer electrolyte fuel cells. *J Electrochem Soc* 2007;154(2):B147. <https://doi.org/10.1149/1.2402124>.
- [34] Jiao K, Li XG. Water transport in polymer electrolyte membrane fuel cells. *Prog Energy Combust Sci* 2011;37:221–91.
- [35] Ko J, Ju H. Comparison of numerical simulation results and experimental data during cold-start of polymer electrolyte fuel cells. *Appl Energy* 2012;94:364–74.
- [36] Yang ZR, Du Q, Huo S, Jiao K. Effect of membrane electrode assembly design on the cold start process of proton exchange membrane fuel cells. *Int J Hydrogen Energy* 2017;42:25372–87.
- [37] Ye Q, Nguyen TV. Three-dimensional simulation of liquid water distribution in a pemfc with experimentally measured capillary functions. *J Electrochem Soc* 2007;154(12):B1242. <https://doi.org/10.1149/1.2783775>.
- [38] Springer TE, Zawodzinski TA, Gottesfeld S. Polymer electrolyte fuel-cell model. *J Electrochem Soc* 1991;138:2334–42.
- [39] Ju H, Wang C-Y, Cleghorn S, Beuscher U. Nonisothermal modeling of polymer electrolyte fuel cells - I. Experimental validation. *J Electrochem Soc* 2005;152(8):A1645. <https://doi.org/10.1149/1.1943591>.
- [40] Mao L, Wang C-Y, Tabuchi Y. A multiphase model for cold start of polymer electrolyte fuel cells. *J Electrochem Soc* 2007;154(3):B341. <https://doi.org/10.1149/1.2430651>.
- [41] Thompson EL, Capehart TW, Fuller TJ, Jorne J. Investigation of low-temperature proton transport in Nafion using direct current conductivity and differential scanning calorimetry. *J Electrochem Soc* 2006;153(12):A2351. <https://doi.org/10.1149/1.2359699>.
- [42] Kandlikar SG, Lu ZJ. Fundamental research needs in combined water and thermal management within a proton exchange membrane fuel cell stack under normal and cold-start conditions. *J Fuel Cell Sci Technol* 2009;6:13.
- [43] Jiao K, Li XG. Effects of various operating and initial conditions on cold start performance of polymer electrolyte membrane fuel cells. *Int J Hydrogen Energy* 2009;34:8171–84.
- [44] Kulikovskiy AA. Analytical modelling of fuel cells. 1st ed. UK: Elsevier; 2010.
- [45] Tajiri K, Tabuchi Y, Kagami F, Takahashi S, Yoshizawa K, Wang CY. Effects of operating and design parameters on PEFC cold start. *J Power Sources* 2007;165:279–86.
- [46] Jiang F, Wang C-Y, Chen KS. Current ramping: a strategy for rapid start-up of pemfcs from subfreezing environment. *J Electrochem Soc* 2010;157(3):B342. <https://doi.org/10.1149/1.3274820>.
- [47] Wei L, Dafalla AM, Jiang FM. Effects of reactants/coolant non-uniform inflow on the cold start performance of PEMFC stack. *Int J Hydrogen Energy* 2020;45:13469–82.